

ANALYTICAL MODELLING BASED ON RESONANCE SCATTERING THEORY EXPLAINING THE NEEDLE VISIBILITY INCONSISTENCY IN B-MODE ULTRASOUND

Hesty Susanti^{1*}, S. Suprijanto², Deddy Kurniadi²

¹ School of Electrical Engineering, Telkom University, Bandung, Indonesia

e-mail: hestysusanti@telkomuniversity.ac.id

² Instrumentation and Control Research Group, Faculty of Industrial Technology, Bandung, Indonesia

e-mail: supri@tf.itb.ac.id, kurniadi@tf.itb.ac.id

* *corresponding author*

Abstract

In an ultrasound-guided needle insertion, physicians should adjust a certain insertion angle and the position of the transducer to ensure that the initial point and final target are in-plane inside the imaging plane. One of the crucial problems in this interventional procedure is poor and inconsistent needle visibility in B-mode ultrasound. In this research, some potential physical parameters, i.e., ultrasound frequency, the incident angle of the ultrasound beam, needle density, and dimension, are investigated through analytical modeling based on the resonance scattering model to understand their behavior in affecting needle visibility. 25G non-echogenic needle is used as a model object and assumed as stainless-steel hollow cylinder insonified by oblique incident plane wave varied within the frequency of 0–10 MHz and incident angle of 0°–45°. The results suggest that those physical parameters simultaneously affect the occurrence possibility of the resonant modes, which eventually affect the total scattering pressure field P_s in a non-linear way. These observed behaviors in the form of the spectrum map of resonance scattering pressure amplitude can be used to adapt a more beneficial combination of those physical parameters to obtain a higher possibility of good needle visibility through practical insertion application and potential echogenic technology or adaptive beamforming.

Keywords: Analytical modeling, interventional procedure, needle visibility, resonance scattering, ultrasound

1. Introduction

In the medical world, the minimally invasive interventional procedure is defined as a treatment or diagnostic procedure involving the insertion process of tools into the body or body cavity, which emphasizes minimizing injury. This procedure usually involves a needle in its application, e.g., in anesthesia and biopsy. For ensuring a successful procedure, visual feedback for physicians is strongly needed. One of the imaging modalities that is used for guiding the needle is ultrasonography. This modality is chosen because it has high temporal resolution and no radiation

risk, relatively small transducer and equipment, and the availability of multiple imaging planes of approach.

In ultrasound imaging for needle guiding application, the physicians must adjust a certain insertion angle and the position of the transducer to ensure the initial point of insertion and final target of the needle in order for it to be in-plane in the imaging plane.

In an ideal condition, the visibility of the needle is expected to be clearly visualized in the defined imaging plane with the variation of depth and insertion angles relative to the initial point of insertion and transducer type. However, in clinical application, the advantage of ultrasound also comes with another consequence, i.e., poor, and inconsistent needle visibility in the B-mode image. In previous studies, poor needle visibility has been reported to hinder the performance of needle insertion procedures (de Jong et al. 2018; Susanti et al. 2018). Some technical factors, e.g., ultrasound frequency and insertion angle, affect it, but no linearity has been found. For example, in Fig. 1, at 15° , the needle shaft can be imaged fully, but at 25° , only the middle part is visualized more clearly.

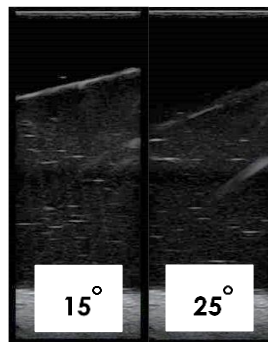


Fig. 1. Inconsistency of needle visibility in B-mode image in various insertion angles.

1.1 Works related to needle visibility

Previously, the inconsistency of needle visibility encountered in clinical application encourages the studies of the quantification of needle visibility in the B-mode images. A relative contrast of needle image is evaluated based on the scoring system through direct visual observation by physicians (Rominger et al. 2017). The assessment of scoring data is evaluated and justified by applying statistics to evaluate the significance of imaging strategies, needle type, and the relative position of the needle to the ultrasound beam on the quality of needle visibility. However, those scoring systems have limitations in combining physical parameters in the experimental settings to give a general conclusion in needle visibility problems.

Other methods have been developed to quantify needle visibility through post-image processing strategies (van de Berg et al. 2019; Xu et al. 2018). The main idea behind mentioned methods is to identify some points along the needle shaft with good contrast relative to the background. These points are viewed as featured data sets of needles. Using supporting information, e.g., the tail effect contrast on needle tip and needle insertion angle, image processing algorithms have been proposed to visualize “virtual needle” as interpolation of featured data set that have a close correlation with the needle in the B-mode ultrasound. Then, the “virtual needle” is superimposed with a measured B-mode image. Real-time application of this post-processing approach is still limited. It works well in a specific condition and often requires a high computation load.

After quantifying needle visibility, studies related to needle visibility are then carried out with re-engineering approaches to increase needle visibility. Generally, those researches can be categorized into three categories regarding the aspects of the system, i.e., the source (the imaging strategy), the object (the needle), and the interaction between the source and the object (the relative position of the needle to the ultrasound beam).

In the first category, the engineering is performed in the imaging strategy. Using a phased array transducer, some researchers attempt to develop beamforming strategies (Prabhakar et al. 2018) to maximize received beams from the backpropagation of the needle. Another imaging strategy called compound imaging is also investigated (Wiesmann et al. 2013). The 3D ultrasound is also used to solve the inconsistency of needle visibility (Arif et al. 2018).

In the second category, the engineering is carried out on the needle as the object to be imaged, including the modification of acoustic characteristics, geometry, and the needle's surface. The echogenic technology belongs to this category by dimpling, roughening, coating, or their combinations on the outer surface of the needle (Brookes et al. 2015; Tang et al. 2016) to maximize the amount of backpropagation received by the transducer through specular reflection.

In the third category, the engineering is performed on the interaction parameters between the wave source and the object, i.e., the relative position of the needle to the ultrasound beam, including the incident angle of the ultrasound beam and the depth of insertion. An example of this interaction category is the utilization of a needle-guide kit to stabilize the needle (Ueshima and Kitamura 2015; Yoshimimura et al. 2016), and the technique of needle insertion, including in-plane and out-of-plane insertion technique (Maddali et al. 2017).

2. Methodology

2.1 Modelling concepts and objective

A better understanding of the problem of needle visibility can be achieved if backpropagation is only due to the needle being isolated. Immersing needles in the water is one approach to obtain a homogeneous and anechoic background environment. The modeling concepts of this system are shown in Fig. 2. Recalling the basic principle of ultrasound imaging, when m -element of the transducer is triggered, an ultrasound wave propagates through the water and eventually arrives on the needle's surface (Fig. 2a). Due to the interaction between the incident wave and the needle, the backpropagation pressure field is received by the transducer and converted into A-mode in each scan line (Fig. 2b). The maximum amplitude of the signal received by each element is proportional to the amount of backpropagation. Using information from m -element of the transducer, reconstruction of the needle on a B-mode image can be obtained (Fig. 2c).

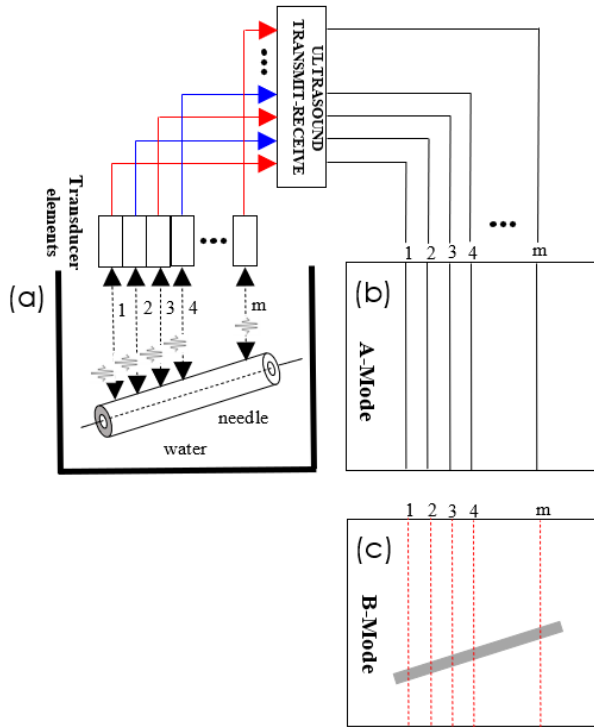


Fig. 2. The modeling concept of the system: (a) pulse-echo process, where m -element transducer transmits and receives ultrasound signal to and from the media (water and needle), (b) A-mode for each scan-line, (c) B-mode image of the needle.

Based on this imaging concept, the inconsistency of needle visibility closely relates to the amplitude of the backpropagation pressure field received by the transducer. From previous related works, we can summarize that the amplitude of the backscattering pressure field is influenced by several physical parameters, i.e., the frequency of ultrasound wave as the source parameter, the material properties and dimension of the needle as object parameters, and the incident angle of ultrasound beam as the parameter of interaction between the source and the object.

A comprehensive evaluation of the needle visibility problems using an experimental approach is tricky because it needs a tremendous number of measurements to variate every possibility of combining the system's parameters.

Although acoustic wave propagation through an elastic cylindrical object has been investigated extensively in the literature considering many different cases, its application for ultrasound-guided needle insertion is still limited. Previous studies approached this case with modeling approaches, such as finite element modeling (Bigeleisen et al. 2016; Kuang et al. 2016), which suggests that computational load requires a more significant number of grid points per wavelength to avoid numerical dispersion.

In this research, we propose an alternative evaluation approach to understand better the fundamental physics that underlie the inconsistency of needle visibility through analytical modeling of ultrasound wave propagation. Compared to finite element modeling, this analytical model requires less computational load. From this approach, the physical parameters that influence backscattering pressure amplitude will be evaluated. The model is developed based on

the phenomenon of resonance scattering response from a stainless-steel hollow cylinder insonified by an oblique incident plane wave.

Compared to our proposed model, the model proposed by Kuang *et al* (Kuang et al. 2016) is employed to an ultrasound-actuated needle, while in our model, the needle is assumed to be static or vibrationless. The ultrasound-actuated needles can cause tissue motion beyond the needle shaft and tip, making it challenging to locate the tip precisely. Therefore, a static or vibrationless needle is preferably used in clinical applications. Another modeling approach proposed by Bigeleisen *et al* (Bigeleisen et al. 2016) is applied to the echogenic needle, while in our case the needle is non-echogenic and is used more commonly than the echogenic needle.

The analytical model is designed to take the whole aspects of the system into account to support the research's objectives, i.e., the source, the object, and the interaction parameter between the source and the object. In the proposed analytical model, each scattering amplitude from each scan-line due to the interaction between the incident wave and the needle contributes to the total scattering pressure amplitude. Numerical simulation is performed to obtain the solution of the analytical model of resonance scattering with the parameters mimicking the condition in clinical application.

2.2 Mathematical model

The spinal needle has two main parts, i.e., stylet and the needle shaft. The object used in the proposed model is the needle shaft (Fig. 3b) which can be approximated as a stainless-steel hollow cylinder.

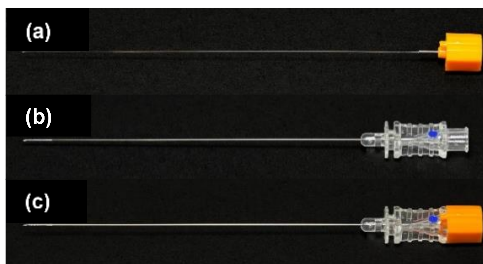


Fig. 3. 25G standard non-echogenic spinal needle and its parts: (a) the stylet (rigid cylinder), (b) the needle shaft (hollow cylinder), (c) the stylet attached to the needle shaft (rigid cylinder).

From the modeling concept illustrated in Fig. 2, the transducer is assumed to generate a plane wave insonifying a stainless-steel hollow cylinder obliquely to the object's axis.

2.3 Works related to acoustic wave propagation through the elastic cylindrical object

The theory of acoustic scattering response from cylindrical objects has been introduced in previous works (Fan et al. 2003; Flax et al. 1978; Leon et al 1992). Those works have laid the fundamental theory on how the acoustic wave behaves through a cylindrical object (rigid or hollow) by responding in resonance scattering in specific wave modes. A stainless-steel hollow cylinder can be viewed as an elastic medium; therefore, mechanical properties, i.e., Young's modulus, Poisson's ratio, density, and dimension, must be considered in the acoustic characteristics of wave propagation in it.

2.4 Analysis of mathematical model

To derive a rigorous analytical model supporting the research’s objectives, the modeling concept that focused on the immersed needle in a water chamber is illustrated in Fig. 4. In this case, the system is divided into three media, i.e., water as medium 1, stainless-steel shell as medium 2, and air inside the needle as medium 3.

Suppose that the P_0 is the amplitude of the plane wave as the incident wave, the pressure field at a point in medium 1 is the sum of the incident wave P_i and scattering wave P_s represented by

$$P_i = P_0 \sum_{n=0}^{\infty} \epsilon_n i^n J_n(k_{\perp} r) \cos(n\theta) e^i(k_z z - \omega t) \tag{1}$$

$$P_s = P_0 \sum_{n=0}^{\infty} \epsilon_n i^n g_n H_n^{(1)}(k_{\perp} r) \cos(n\theta) e^i(k_z z - \omega t) \tag{2}$$

Where n is order number, ϵ_n is Neumann factor, which is $\epsilon_n = 1 (n = 0)$ or $\epsilon_n = 2 (n \neq 0)$; J_n is Bessel function of the first kind and $H_n^{(1)}$ is Hankel function of the first kind with order n , and k is wave number. P_i hits the surface of the needle and interacts with the solid material of the stainless-steel cylindrical shell resulting in an outgoing scattering pressure field P_s .

P_s represents the total scattering pressure field received by the transducer. Water as a background medium is considered as an anechoic medium, so backpropagation received by the transducer is assumed to be only from the scattering pressure field P_s of the needle.

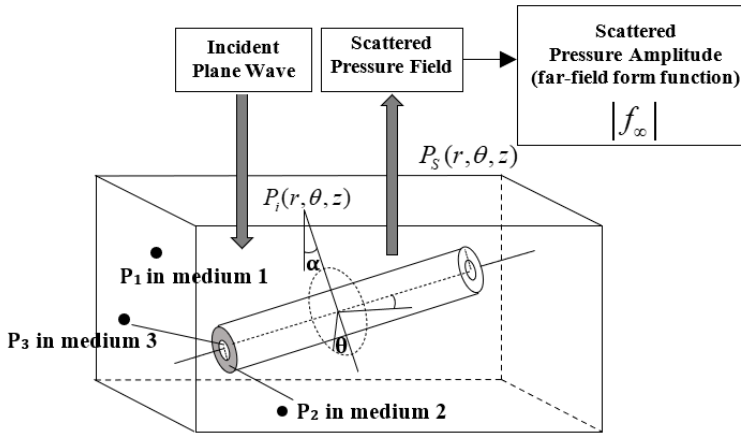


Fig. 4. The modeling concept that focuses on an immersed needle in a water chamber.

The solutions of the governing of wave equations must be solved at each domain of the system (see the cross-section of the cylinder and background media in Fig. 5) to determine g_n as the unknown scattering coefficient of P_s . The governing of wave equations for medium 1, medium 2, and medium 3 are summarized in Table 1.

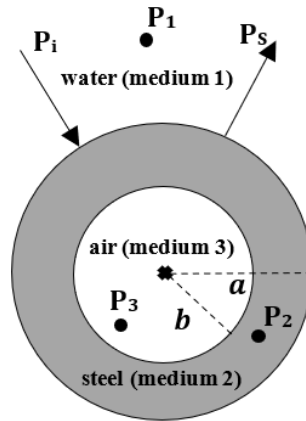


Fig. 5. Cross-section of a hollow cylinder and background media, with the distribution of pressure fields.

Medium	Governing equations
Medium 1: Water c_1 : sound speed in the water ρ_1 : water density	$\nabla^2 \phi_1 - \frac{1}{c_1^2} \frac{\partial^2 \phi_1}{\partial t^2} = 0 \quad (3)$ ϕ_1 : scalar potential
Medium 2: Stainless-steel shell c_L : sound speed of the longitudinal wave in steel c_T : sound speed of the transversal wave in steel ρ_2 : steel density	$\nabla^2 \phi_2 - \frac{1}{c_L^2} \frac{\partial^2 \phi_2}{\partial t^2} = 0 \quad (4)$ $\nabla^2 \Psi - \frac{1}{c_T^2} \frac{\partial^2 \Psi}{\partial t^2} = 0 \quad (5)$ ϕ_2 : scalar potential Ψ : vector potential $\Psi = \Psi_r + \Psi_\theta + \Psi_z \quad (6)$
Medium 3 c_3 : sound speed in the air ρ_3 : air density	$\nabla^2 \phi_3 - \frac{1}{c_3^2} \frac{\partial^2 \phi_3}{\partial t^2} = 0 \quad (7)$ ϕ_3 : scalar potential

Table 1. The governing wave equations at each domain of the system.

At medium 1 (water), the resultant pressure field at a certain point 1 is the function of scalar displacement potential ϕ_1 as the solution of Eq. 3. At medium 2 (stainless-steel shell), the interaction between the incident wave and the material of the cylinder causes the excitation of the vibrational displacement u formulated as (Morse and Feshbach 1953):

$$u = \nabla \phi_2 + \nabla \times \Psi \quad (8)$$

Eq. 8 are satisfied if ϕ_2 and Ψ verify the Eq. 4-5. In medium 3 (air), the pressure field at a certain point 3 is the function of scalar displacement potential ϕ_3 as the solution of Eq. 7. The general solution of $\phi_1, \phi_2, \Psi_r, \Psi_\theta, \Psi_z$ and ϕ_3 can be expressed as:

$$\phi_1 = -\frac{1}{\rho_1 \omega^2} \sum_{n=0}^{\infty} \epsilon_n i^n [J_n(k_{\perp} r) + g_n H_n^{(1)}(k_{\perp} r)] \times \cos(n\theta) \exp[i(k_z z - \omega t)] \quad (9)$$

$$\phi_2 = \sum_{n=0}^{\infty} [a_n U_n(hr) + b_n V_n(hr)] \cos(n\theta) \Omega_n \quad (10)$$

$$\Psi_r = \sum_{n=0}^{\infty} [c_n U_{n+1}(Kr) + d_n V_{n+1}(Kr)] \sin(n\theta) \Omega_n \quad (11)$$

$$\Psi_{\theta} = \sum_{n=0}^{\infty} [-c_n U_{n+1}(Kr) - d_n V_{n+1}(Kr)] \cos(n\theta) \Omega_n \quad (12)$$

$$\Psi_z = \sum_{n=0}^{\infty} [e_n U_n(Kr) + f_n V_n(Kr)] \sin(n\theta) \Omega_n \quad (13)$$

$$\phi_3 = -\frac{1}{\rho_3 \omega^2} \sum_{n=0}^{\infty} \epsilon_n i^n q_n J_n(k_3 r \cos \alpha) \times \cos(n\theta) \exp[i(k_z z - \omega t)] \quad (14)$$

where,

$$\Omega_n = \left(\frac{1}{\rho_2 \omega^2} \right) \epsilon_n i^n \exp[i(k_z z - \omega t)] \quad (15)$$

$$h^2 = \frac{\omega^2}{c_L^2} - k_z^2 \quad (16)$$

$$K^2 = \frac{\omega^2}{c_T^2} - k_z^2 \quad (17)$$

The solutions include the terms U_n and V_n which represent the Bessel function of the first kind (J_n), and second kind (N_n), or the modified Bessel function of the first kind (I_n) and second kind (K_n). They depend on the angle of incident, affecting the solution of Eq. 16-17, which can be real or imaginary.

The total solutions of the whole system consist of 6 general solutions (Eq. 9-14) with 8 unknown coefficients a_n , b_n , c_n , d_n , e_n , f_n , g_n and q_n . These solutions are then substituted into the boundary conditions at the interface of the domains $r = a$ and $r = b$:

- Continuity of the radial displacements:

$$r = a, u_{r1} = u_{r2} \quad (18)$$

$$r = b, u_{r2} = u_{r3} \quad (19)$$

- Continuity of the radial stresses:

$$r = a, T_{rr1} = T_{rr2} \quad (20)$$

$$r = b, T_{rr2} = T_{rr3} \quad (21)$$

- Nullity of the tangential and shear stresses:

$$r = a, T_{r\theta 1} = T_{rz 2} = 0 \tag{22}$$

$$r = b, T_{r\theta 2} = u_{rz} = 0 \tag{23}$$

By substituting those solutions into the boundary conditions at $r = a$ and $r = b$, the system of 8 linear homogeneous equations can be represented as:

$$M \cdot A = B \tag{24}$$

$$\begin{bmatrix} M_{11} & M_{12} & M_{13} & M_{14} & M_{15} & M_{16} & M_{17} & M_{18} \\ M_{21} & M_{22} & M_{23} & M_{24} & M_{25} & M_{26} & M_{27} & M_{28} \\ M_{31} & M_{32} & M_{33} & M_{34} & M_{35} & M_{36} & M_{37} & M_{38} \\ M_{41} & M_{42} & M_{43} & M_{44} & M_{45} & M_{46} & M_{47} & M_{48} \\ M_{51} & M_{52} & M_{53} & M_{54} & M_{55} & M_{56} & M_{57} & M_{58} \\ M_{61} & M_{62} & M_{63} & M_{64} & M_{65} & M_{66} & M_{67} & M_{68} \\ M_{71} & M_{72} & M_{73} & M_{74} & M_{75} & M_{76} & M_{77} & M_{78} \\ M_{81} & M_{82} & M_{83} & M_{84} & M_{85} & M_{86} & M_{87} & M_{88} \end{bmatrix} \begin{bmatrix} a_n \\ b_n \\ c_n \\ d_n \\ e_n \\ f_n \\ g_n \\ q_n \end{bmatrix} = \begin{bmatrix} B_1 \\ 0 \\ B_3 \\ 0 \\ 0 \\ 0 \\ 0 \\ 0 \end{bmatrix} \tag{25}$$

The expressions for element M_{ij} and B_i can be found in Leon *et al.* (Leon et al. 1992).

2.5 Numerical simulation

The physical parameters of each medium are given in Table 2. Those parameters are required to calculate the elements of M_{ij} and B_i . The solution of scalar potential ϕ_1 can be determined entirely by solving Eq. 24-25 using specific frequency ($\omega/2\pi$) of incident plane wave and angle of the incident wave (α).

$$A = M^{-1}B \tag{26}$$

Furthermore, scattering coefficient g_n is related to the element A_7 of the matrix A in the solution.

Medium	Physical parameters
Medium 1: water	$c_1 = 1492$ m/s; $\rho_1 = 1000$ kg/m ³
Medium 2: stainless-steel type 316 (Standard non-echogenic spinal needle) size: 25G	Young's modulus $E = 200$ GPa Shear modulus $\mu = 78.14$ GPa $\rho_2 = 8027$ kg/m ³ $c_L = 5664$ m/s $c_T = 3120$ m/s Outer radius $b = 0.51$ mm Inner radius $a = 0.26$ mm Length $L = 90$ mm
Medium 3: air	$c_3 = 330$ m/s; $\rho_3 = 1.2$ kg/m ³

Table 2. Physical parameter of each medium.

Based on the acoustic properties of the needle, in the specific incident angles (α), the matrix M becomes nearly singular. The roots of the determinant of the matrix M are eigenvalues related to the hollow cylinder's circumferential resonance frequencies. The term critical angles are introduced based on the acoustic properties of the needle, which will characterize the behavior of specific circumferential wave modes that are responsible for the generation of resonances. The whispering gallery wave associated with helical waves is excited up to the critical angle α_l , called the angle of a longitudinal wave in thin rods. The second type of whispering gallery wave is helical guided waves which are excited up to the critical angle α_T . (Fan et al. 2003)

$$\alpha_l = \sin^{-1} \left(\frac{c_{water}}{\sqrt{\frac{E}{\rho_{steel}}}} \right) \quad (27)$$

$$\alpha_T = \sin^{-1} \left(\frac{c_{water}}{\sqrt{\frac{\mu}{\rho_{steel}}}} \right) \quad (28)$$

The scattering pressure field P_s received by the transducer is assumed to be present in the far-field of the cylinder ($r \gg a$) at a specific incident angle α and frequency range f . Far-field scattering pressure field can be expressed as:

$$P_s \approx \sqrt{\frac{2}{\pi k_{\perp} r}} \exp[i(k_{\perp} r + k_z z - \pi/4)] \sum_{n=0}^{\infty} \epsilon_n g_n \cos(n\theta) \quad (29)$$

Leon *et al* (Leon et al. 1992) introduce the far-field form function as the resulting far-field amplitude spectrum by keeping the definition used by Flax *et al* (Flax et al. 1978):

$$|f_{\infty}| \approx \left(\frac{2r}{a} \right)^{1/2} \left| \frac{P_s}{P_i} \right| \quad (30)$$

The far-field form function can be written as the sum of the modeling normal modes:

$$|f_{\infty}| \approx \frac{2}{\sqrt{\pi k_{\perp} a}} \left| \sum_{n=0}^{\infty} \epsilon_n g_n \cos(n\theta) \right| \quad (31)$$

Recalling the modeling concept illustrated in Fig. 2, the far-field scattering amplitude $|f_{\infty}|$ at a specific incident angle α and frequency range f is proportional to the backscattering pressure field received by each transducer element.

The total scattering pressure field P_s consists of the resonance component and non-resonant background. In this case, only the resonance component will be evaluated because it primarily causes the inconsistency of needle visibility (Dencks et al. 2014). The spectrum of the resonance scattering pressure field can be determined by removing the non-resonant background. The scattering coefficient of rigid or non-resonant background is defined as follows (Flax et al 1978):

$$g_n^{rigid}(ka) = \frac{J_n'(ka)}{H_n^{(1)'}(ka)} \quad (32)$$

Here, J_n' is the derivative of the Bessel function of the first kind, while $H_n^{(1)'}$ is the derivative of the Hankel function of the first kind.

In clinical application, the spectrum of resonance scattering pressure amplitude is represented as the areas on B-mode images with good needle visibility. Therefore, the potential physical parameters that can be modified to enhance the possibility of resonance are needed to be observed.

2.6 Algorithm of the simulation

The calculation of resonance component of far-field form function $|f_\infty|$ will be divided into the following steps:

- | | |
|---------|--|
| Step 1 | Input parameters ϵ_n and n |
| Step 2 | Input parameters of background media: ρ_{water} , c_{water} , ρ_{air} , c_{air} |
| Step 3 | Input parameters of stainless-steel needle: L , a , b , ρ_{steel} , α , E , c_L , c_T , μ |
| Step 4 | Calculate critical angles α_l and α_T |
| Step 5 | Discretization of f frequency (idx). Resolution: 0.1 MHz |
| Step 6 | Discretization of incident angle α (idy). Resolution: 0.1° |
| Step 7 | Calculate angular frequency ω and h , K |
| | Note: h and K are different for each condition of incident angle that affect the elements of matrix M and B (see Eq. 24-25): |
| | Condition 1 ($\alpha < \alpha_l$); Condition 2 ($\alpha_l < \alpha < \alpha_T$); Condition 3 ($\alpha > \alpha_T$) |
| Step 8 | Calculate elements of matrix M and B of Eq. 24-25 |
| Step 9 | Calculate elements of matrix A : $A = M^{-1}B$ |
| Step 10 | Calculate resonance component of far-field form function of each frequency: $ f_\infty $ (idx) |
| Step 11 | Calculate resonance component of far-field form function of each incident angle within the frequency range: $ f_\infty $ (idy) |

The simulation is run in MATLAB® (R2016b, The MathWorks, Natick, USA). The calculation of the element of matrix A in step 9 involves the inversion process of matrix M with the LU decomposition method. This method is used to invert nearly singular matrix M , where MATLAB® displays a warning message but performs the calculation to obtain the solution regardless. All values of resonance component of far-field form function $|f_\infty|$ for every couple of α and f are then depicted in the given range of incident angle α and frequency f .

3. Results and discussion

The spectrum of resonance scattering pressure amplitude distribution is then observed within the frequency range of 0–10 MHz and incident angle of 0° – 45° . For general observation, the simulation is performed for a 25G standard non-echogenic spinal needle.

Based on the acoustic properties of the needle (stainless-steel type 316), the two critical angles are $\alpha_i = 17.4^\circ$ and $\alpha_T = 27.8^\circ$. These two critical angles determine certain circumferential waves that are responsible for the generation of resonances. At the critical angle, a specific resonance mode can reach its maximum value. At α_i , the wave's longitudinal component which propagates on the needle's surface, while at α_T , the resonance mode is associated with the transversal component of the wave, which propagates into the solid shell of the needle.

The resonance modes that associate with whispering gallery waves (helical waves type) are excited up to the angle of $\alpha_i = 17.4^\circ$, while the whispering gallery waves (helical guided waves type) are excited up to the angle of $\alpha_T = 27.8^\circ$. Leon *et al.* (Leon *et al.* 1992) discussed another wave mode: the transition between whispering gallery wave and guided wave, i.e., the Scholte-Stoneley helical wave. At $\alpha < \alpha_i$, the Scholte-Stoneley waves and the guided waves appear, while the whispering gallery waves disappear. At $\alpha > \alpha_T$, the guided waves disappear, and the Scholte-Stoneley waves remain.

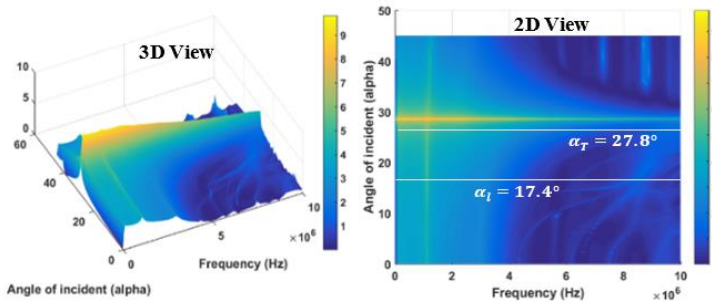


Fig. 6. The spectrum of resonance scattering pressure amplitude for $n = 1-5$.

From Fig. 6, at $\alpha = 28.5^\circ$ that is approaching the second critical angle α_T , there are strong resonance peaks within the entire range of frequencies between 0–10 MHz. At $0 \leq f \leq 3$ MHz, within the entire range of incident angles between 0° – 45° , lower resonance peaks tend to decrease with increasing frequency gradually. At $f \approx 7$ MHz and $f \approx 9$ MHz, there are resonance peaks in the higher range of incident angle, i.e., $\alpha > 30^\circ$. Other resonance peaks vary within the middle range of frequency and lower range of incident angle until approaching the second critical angle α_T .

The simulation is performed by varying the parameters, i.e., inner radius, outer radius, and density, to observe the effect of variation of some potential physical parameters which can be modified to enhance needle visibility. The influences of those parameters are evaluated within the same range of frequency of 0–10 MHz and incident angle of 0° – 45° .

3.1 Variation of the inner radius

The inner radius is simulated for the value of 0.40 mm, 0.26 mm, and 0.01 mm, while the outer radius is constant at 0.51 mm (size 25G). These variations simulate the condition of the hollow dimension, ranging from thinner wall to thicker wall approaching the condition of an approximate rigid cylinder when the stylet is inserted into the needle.

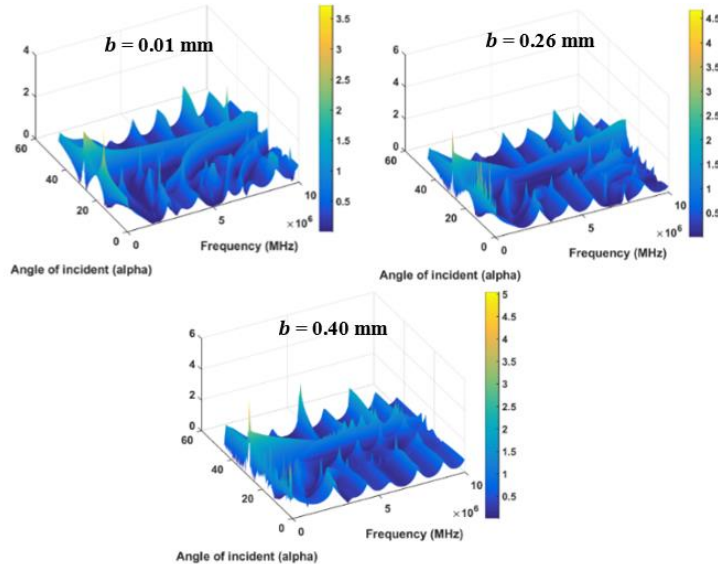


Fig. 7. The spectrum of resonance scattering pressure amplitude for $n = 1$; variation of the inner radius (b).

By varying the inner radius, both for the order $n = 1$ (Fig. 7) and $n = 1-5$ (Fig. 8), within the same range of frequency and incident angle, the distribution of resonance peaks tends to be broader if the inner radius shrinks until the condition approaching the approximate rigid cylinder. The ripples also tend to be smoother and more crowded for the smaller inner radii. In other words, the possibility to obtain a broader area of good needle visibility within a specific range of frequency and incident angle is higher for the needle with a smaller inner radius and approximate rigid cylinder than a hollow cylinder with a bigger inner radius. This result makes it more beneficial for physicians or sonographers for clinical application to image the spinal needle while the stylet is still attached to the hollow cylinder. If the position of the needle relative to the target is already correct, then the stylet can be removed from the hollow cylinder to flow the fluid.

Specifically, for the parameters of outer radius and density, the influences of those parameters to the distribution of resonance scattering pressure amplitude in the mean of their amplitudes and frequency-dependent are evaluated for three representative incident angles, i.e., 10° ($\alpha < \alpha_l$), 25° ($\alpha_l < \alpha < \alpha_T$), and 35° ($\alpha > \alpha_T$) within the same range of frequency of 0–10 MHz.

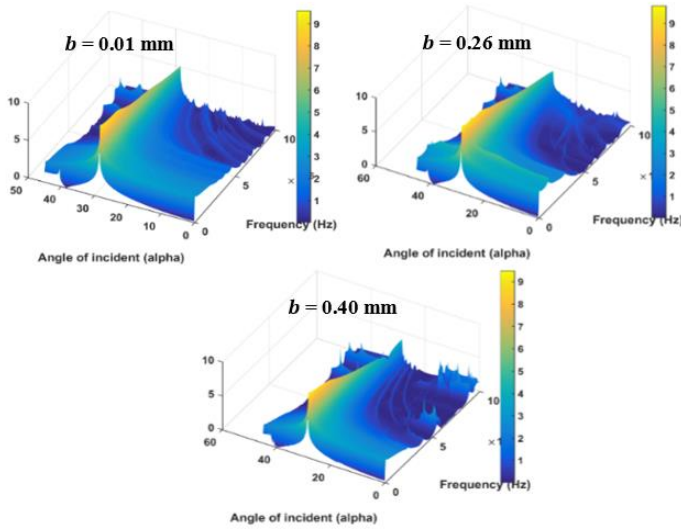


Fig. 8. The spectrum of resonance scattering pressure amplitude for $n = 1-5$; variation of the inner radius (b).

3.2 Variation of the outer radius

The outer radius is simulated for the value of 0.51 mm (original value of size 25G (real)), 0.46 mm (original value -10% (min10)), and 0.56 mm (original value $+10\%$ (plus10)), while the inner radius is maintained to be constant at 0.26 mm (size 25G) and 0.01 mm (approaching the condition of approximate rigid cylinder).

Evaluated from Fig. 9 and Fig. 10, by varying the outer radius, the resonance peaks tend to shift in frequency and fluctuate in amplitude. Both for the inner radius of 0.26 mm and 0.01 mm, the resonance peaks for the outer radius of 0.56 mm lie in the lowest frequency range compared to the resonance peaks for the outer radius of 0.51 mm and 0.46 mm.

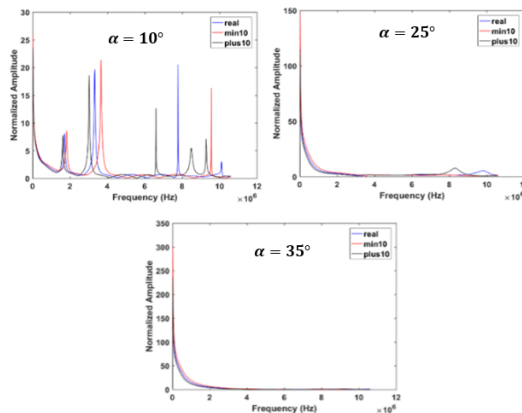


Fig. 9. The spectrum of resonance scattering pressure amplitude, variation of the outer radius (a); $b = 0.26$ mm.

In terms of the amplitude, for the inner radius of 0.26 mm, the amplitude of the resonance for the outer radius of 0.46 mm tends to be the highest among the others. While for the inner radius of 0.01 mm, the resonance amplitude for the outer radius of 0.56 mm tends to be the highest among the others. In other words, the outer radius affects the spectrum of resonance scattering pressure amplitude almost, in the same way, both for standard hollow spinal needle and approximate rigid cylinder.

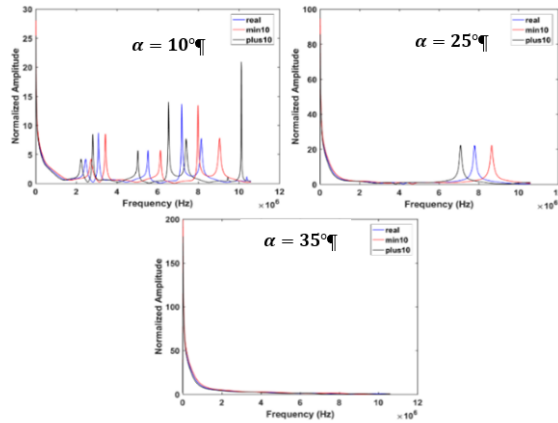


Fig. 10. The spectrum of resonance scattering pressure amplitude, variation of the outer radius (a) ; $b = 0.01$ mm.

3.3 Variation of the density

The density of the needle is simulated for the value of 8027 kg/m^3 (original value of stainless-steel type 316 (real)), 7224.3 kg/m^3 (original value -10% (min10)), and 8829.7 kg/m^3 (original value $+10\%$ (plus10)), while the inner radius is maintained to be constant at 0.26 mm (size 25G) and 0.01 mm (approaching the condition of approximate rigid cylinder).

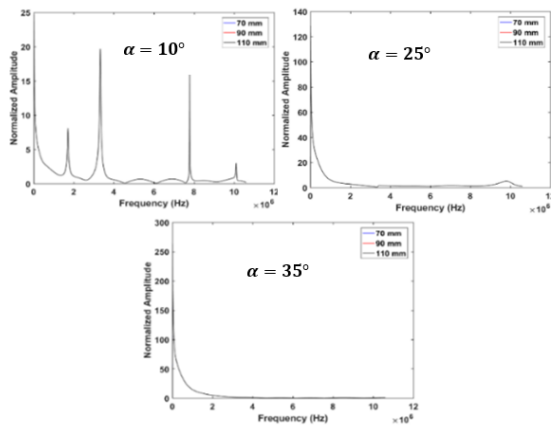


Fig. 11. The spectrum of resonance scattering pressure amplitude, variation of the density (ρ) ; $b = 0.26$ mm.

Evaluated from Fig. 11 and Fig. 12, by varying the density, the resonance peaks tend to fluctuate in amplitude. Both for the inner radius of 0.26 mm and 0.01 mm, the resonance amplitude for the density of 8829.7 kg/m^3 tends to be the highest compared to the resonance peaks for density of 8027 kg/m^3 and 7224.3 kg/m^3 .

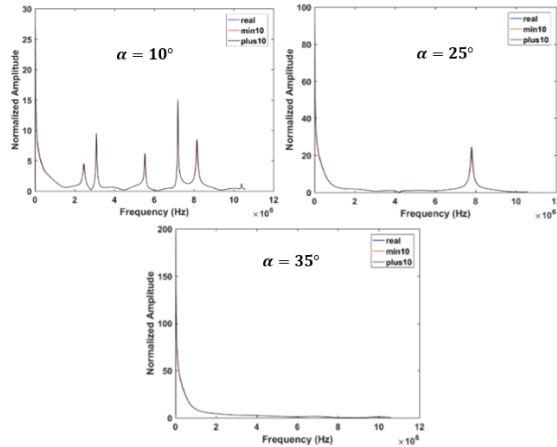


Fig. 12. The spectrum of resonance scattering pressure amplitude, variation of the density (ρ); $b = 0.01 \text{ mm}$.

While in terms of frequency, both for the inner radius of 0.26 mm and 0.01 mm, the resonance peaks lie in the same frequency for all density values. In other words, the density affects the spectrum of resonance scattering pressure amplitude in the same way, both for the standard hollow spinal needle and approximate rigid cylinder.

3.4 Overall discussion

The observation of the spectrum of resonance scattering pressure amplitude within the range of frequency between 0–10 MHz and incident angle of 0° – 45° shows that the resonances associated with specific wave modes vary broadly within the range with the tendency of slight variation above the frequency of 4 MHz. The behavior of specific circumferential wave modes concerning critical angles α_i and α_r depends not only on the frequency and incident angle but also on the radius and density of the needle, where physical interactions occur among the waves generated on the surface and within the solid shell.

As the source parameter, the frequency f of the incident wave P_i affects the angular frequency ω which eventually affects the waves' phase, i.e., the incident wave itself, the scalar potential in the water ϕ_1 , and in the air inside the needle ϕ_3 . Within the solid shell of the needle, frequency f affects the parameters Ω_n , h , and K for the scalar potential ϕ_2 and vector potential Ψ .

Similar to the frequency f , as the parameter of interaction between the source and the object, the incident angle α affects the wavenumber of the waves represented by the parameters k_\perp and k_z which eventually affects the phase of the waves, i.e., the incident wave itself, the scalar potential in the water ϕ_1 , and in the air inside the needle ϕ_3 . Within the solid shell of the needle,

the angle of incident α affects the parameters Ω_n , h , and K for the scalar potential ϕ_2 and vector potential Ψ .

While, as the object parameter, the dimension of the cylinder, i.e., the proportion between inner b and outer radius a affects the acoustic path passed by the waves. The thicker the wall of the cylinder, the larger the acoustic path, so the resonance interactions occur more intensely, represented by the presence of more crowded resonance peaks (Fig. 7 and Fig. 8). This interaction was also observed in a rigid cylinder, where the bigger the outer radius of the rigid cylinder, the higher the chance to find the peak of the resonances (Susanti et al 2018). The outer radius and the density of the needle affect the distribution of the resonance spectrum pressure field in terms of frequency and amplitude, almost in the same way.

4. Conclusions

The accumulation of the influence of those three representative parameters, i.e., the frequency, the incident angle of the ultrasound beam, and the density and dimension of the needle, affects the occurrence possibility of the resonant modes in a non-linear way which eventually affects the total scattering pressure field P_s received by the transducer as backpropagation. In other words, those parameters play essential roles in the generation of visibility of the needle.

Extracted from the P_s by removing non-resonant background, the spectrum of resonance scattering pressure amplitude allows one to observe a specific range of frequency range and incident angle in practical application to adapt a more beneficial combination of those parameters to obtain a higher possibility of good needle visibility using practical insertion application or adaptive beamforming. While the object parameters of the needle, i.e., the inner radius, the outer radius, and the density, can be modified in such a way (echogenic technology) to enhance needle visibility in the B-mode image.

Acknowledgments The authors acknowledge the Indonesia Endowment Fund for Education (LPDP) for providing scholarship for this research and The Ministry of Research, Technology and Higher Education of the Republic of Indonesia for competency-based research funding.

References

- Arif M, Moelker A, van Walsum T (2018). Needle Tip Visibility in 3D Ultrasound Images. *Cardiovascular and Interventional Radiology*, 41, 145-152.
- Bigeleisen P E, Hess A, Zhu R, Krediet A (2016). Modeling, Production, and Testing of An Echogenic Needle for Ultrasound-guided Nerve Blocks. *Journal of Ultrasound in Medicine*, 35, e35-e39.
- Brookes J, Sondekoppam R, Armstrong K, Uppal V, Dhir S, Terlecki M, Ganapathy S (2015). Comparative Evaluation of the Visibility and Block Characteristics of a Stimulating Needle and Catheter vs An Echogenic Needle and Catheter for Sciatic Nerve Block with A Low-Frequency Ultrasound Probe. *British Journal of Anaesthesia*, 115 (6), 912-19.
- de Jong T L, van de Berg N J, Tas L, Dankelman J, van den Dobbelsteen JJ (2018). Needle Placement Errors. Do We Need Steerable Needles in Interventional Radiology? *Medical Devices: Evidence and Research*, 11, 259-265.
- Dencks S, Susanti H, Schmitz G (2014). Needle Visibility for Deep Punctures with Curved Arrays. *Proceedings of IEEE International Ultrasonics Symposium*, 1880-1883.

- Fan Y, Honarvar F, Sinclair A N, Jafari M R (2003). Circumferential Resonance Modes of Solid Elastic Cylinders Excited by Obliquely Incident Acoustic Waves. *Journal Acoustical Society of America*, 113(1), 102-113.
- Flax L, Dragonette L R, Überall H (1978). Theory of Elastic Resonance Excitation by Sound Scattering. *Journal Acoustical Society of America*, 63(3), 723-731.
- Flax L, Varadan V K, Varadan V V (1980). Scattering of An Obliquely Incident Acoustic Wave by An Infinite Cylinder. *Journal Acoustical Society of America*, 68(6), 1832-1835.
- Kuang Y, Hilgers A, Sadiq M, Cochran S, Corner G, Huang Z (2016). Modeling and Characterisation of An Ultrasound-actuated Needle for Improved Visibility in Ultrasound-guided Regional Anesthesia and Tissue Biopsy. *Ultrasonics*, 69, 38-46.
- Leon F, Lecroq F, Decultot D, Maze G (1992). Scattering of An Obliquely Incident Wave by An Infinite Hollow Cylindrical Shell. *Journal Acoustical Society of America*, 91(3), 1388-1397.
- Maddali M M, Arora N R, Chatterjee N (2017). Ultrasound-Guided Out-Of-Plane versus In-Plane Transpectoral Left Axillary Vein Cannulation. *Journal of Cardiothoracic and Vascular Anesthesia*, 31, 1707-1712.
- Morse P M, Feshbach H (1953). Vector fields. In: Morse P M, Feshbach H (ed) *Methods of theoretical physics*. McGraw-Hill, New York, 1764-1767.
- Prabhakar C, Uppal V, Sondekoppam R V (2018). Effect of Beam Steering on Echogenic and Nonechogenic Needle Visibility at 40°, 50°, And 60° Needle Insertion Angles. *Anesthesia and Analgesia*, 126(6), 1926-1929.
- Rominger M B, Martini K, Dappa E, Puippe G, Klingmüller V, Frauenfelder T, Sanabria S J (2017). Ultrasound Needle Visibility in Contrast Mode Imaging: An In Vitro and Ex Vivo Study. *Ultrasound International Open*, 3, E82-E88.
- Susanti H, Suprijanto, Kurniadi D (2018). Two-dimensional Mapping of Needle Visibility with Linear and Curved Array for Ultrasound-guided Interventional Procedure. *AIP Conference Proceedings*, 1933, 040004.
- Tang S J, et al (2016). EUS Needle Identification Comparison and Evaluation Study (with Videos). *Gastrointestinal Endoscopy Journal*, 84(3), 424-433.
- Ueshima H, Kitamura A (2015). The Use of a Needle Guide Kit Improves the Stability of Ultrasound-guided Techniques. *Journal of Anesthesia*, 29(5), 803-804.
- van de Berg N J, Sanchez-Margallo J A, van Dijke A P, Langø T, van den Dobbelsteen J J (2019). A Methodical Quantification of Needle Visibility and Echogenicity in Ultrasound Images. *Ultrasound in Medicine and Biology*, 45(4), 998-1009.
- Wiesmann T, Borntäger A, Zoremba M, Neff M, Wulf H, Steinfeldt T (2013). Compound Imaging Technology and Echogenic Needle Design Effects on Needle Visibility and Tissue Imaging. *Regional Anesthesia and Pain Medicine*, 38(5), 452-455.
- Xu F, Gao D, Wang S, Zhanwen A (2018). MLESAC Based Localization of Needle Insertion using 2D Ultrasound Images. *Journal of Physics: Conference Series*, 1004, 1-9.
- Yoshimimura M, Hayashi M, Numata K, Sakamoto S, Fukuda S, Toriumi S (2016). The Usefulness of Siva Guide® for Beginners Performing Ultrasound-Guided Nerve Block with the In-Plane Approach. *Masui*, 65(10), 1078-1082.